A Sub-20-nW Delay-Encoded IR-UWB Temperature Sensor Utilizing ML-Assisted Voltage Cancellation With Unregulated Supply

Martin Lee and Kambiz Moez, *Senior Member, IEEE*

***Abstract*—This article presents a simplified simultaneous sense-transmit sensor architecture featuring an impulse radio ultra-wideband (IR-UWB) temperature sensor that embeds the sensed temperature directly in the time intervals of an on-off keying (OOK) IR-UWB identifier (ID). Both voltage and temperature (VT) are intrinsically encoded in the intra- and inter-time intervals of the transmitted IR-UWB ID using the inherent dependencies of the core oscillator on these parameters. This eliminates the need for explicit data conversion and minimizes data transmission, simplifying the sensor architecture and significantly reducing power consumption. By designing the sensor to operate with a wide supply voltage range, its energy efficiency is further improved by eliminating the need for voltage regulation. To address the resulting supply-voltage variation, a machine learning (ML) algorithm is applied at the receiver to the time intervals that form a multi-dimensional delay feature space to predict the sensed temperature while cancelling the effects of supply-voltage variation, enabling voltage-insensitive temperature sensing. The proposed sensor is fabricated in TSMC's 130 nm CMOS process and experimentally validated over a temperature range of 10°C to 110°C and a supply voltage range of 1 V to 3 V across six sensors. The IR-UWB temperature sensor achieves an inaccuracy of $\pm$0.22°C (σ) and a mean absolute error (MAE) of 0.16°C, across all temperatures, voltages, and sensors, with a power consumption of 16.7 nW. A fixed systematic polynomial correction reduces the inaccuracy to $\pm$0.19°C (σ) and 0.13°C (MAE).**

***Index Terms*—Impulse radio ultra-wideband (IR-UWB), temperature sensor, machine learning (ML), wireless sensor, delay-encoding, voltage-cancellation, energy harvesting (EH), unregulated supply.**

I. Introduction

THE projected scale of the Internet of Things (IoT) poses significant challenges with powering the vast number of devices over their lifetime. The majority of wireless IoT devices are powered by batteries, necessitating periodic replacement or recharging, a significant barrier to their widespread adoption. This issue can be mitigated by powering devices using energy harvested from external sources such as solar, kinetic, thermal, and radio-frequency (RF) energy. RF energy harvesting (RFEH), in particular, provides a continuously available and easily integrable power source compared to other energy sources. A primary limitation of RFEH IoT devices is their operating range, which is dictated by the trade-off between harvested power and the power consumption of the IoT device. Techniques such as adaptive threshold compensation [1]–[3], maximum power point tracking [4], [5] can increase the harvested energy, however, improvements aimed at reducing the minimum input power level result in low power conversion efficiency (PCE) and are restricted by the transistor's threshold voltage and leakage. At input power levels below -25 dBm, power conversion efficiency (PCE) is typically lower than 10%, yielding an output power on the order of nanowatts [6], [7]. Moreover, the stochastic nature of the received power of RFEH due to varying environmental conditions [8], combined with the severe path loss imposed by the inverse-square law, significantly reduces the available harvested power with distance, forcing a practical compromise between device functionality and operating lifetime. These limitations highlight the need for IoT devices, such as sensors, to operate with extremely low active power to achieve greater energy autonomy.

The total power of a wireless sensor node is divided between sensing and transmission, and treating these two subsystems independently introduces inherent inefficiencies. In conventional architectures, the sensing element and its readout circuitry first convert the environmental quantity into an electrical parameter such as capacitance, resistance, or voltage, which is then digitized by an analog-to-digital converter (ADC) [9]–[11]. Achieving high sensing accuracy typically requires high ADC resolution, resulting in high power consumption [9], [11], [12]. For low-power sensors, time-to-digital converters (TDCs) and frequency-to-digital converters (FDCs) have been investigated, utilizing counter-based architectures that are more energy efficient [13], [14]. Nevertheless, explicit data conversion is still used, and the TDC or FDC can account for a significant fraction of the total sensor power [15]–[17]. Moreover, these approaches often assume the availability of a stable reference clock in IoT nodes, and this can increase power consumption significantly [14], [16], [17]. When integrated into a wireless node, this power overhead is compounded by the additional power requirements for RF modulation and transmission. Sensor data is typically transmitted by digitally modulating a continuous-wave (CW) carrier [18]. Consequently, multiple conversion stages from the sensed environmental quantity to RF modulation are required before the information is transmitted. In widely adopted wireless standards, CW transmitters operate with continuously running oscillators and RF front-ends, making them inherently power-intensive. Although power can be reduced through sleep cycles, the fundamental architecture of CW transmitters renders them unsuitable for very low-power applications. Alternative

The authors are with the Department of Electrical and Computer Engineering, University of Alberta, Edmonton, AB T6G 1H9, Canada e-mail: (mklee@ualberta.ca;kambiz@ualberta.ca).

transmission methods like backscattering can reduce power consumption by modulating the antenna's impedance to reflect incident signals instead of relying on an active transmitter [19]. However, backscattering communication requires the receiver to transmit first to receive sensor information. Consequently, the range is limited by the initial transmit power to the sensor, the limited reflected power from the sensor and two-way path loss. Impulse-radio ultra-wideband (IR-UWB) is a promising alternative [20], [21]. Although it uses an active transmitter, IR-UWB emits nanosecond pulses with a very low duty cycle, enabling long idle periods and substantially lower average power. The pulse transmission also allows for significantly lower design complexity. Developing a wireless sensor that consumes nanowatts of power will necessitate a fundamental shift in architecture and technique.

This article proposes a simplified simultaneous sense-transmit IR-UWB sensor architecture that reduces overall power consumption by integrating sensing and transmission functions to eliminate explicit data conversion and on-sensor voltage regulation, while minimizing transmitted data through the direct encoding of sensed information in the transmission. The sensor transmits a delay-encoded on-off keying (OOK) IR-UWB identifier (ID) using a core oscillator that simultaneously drives the IR-UWB transmitter while intrinsically encoding voltage and sensed data into the intra- and inter-time intervals of the IR-UWB ID. The encoding of sensed data within these time intervals eliminates the transmission of all data bits and the need for on-sensor data conversion. Based on this architecture, a temperature sensor is developed in which the sensed temperature is embedded directly within the transmission, leveraging the inherent dependency of the ring oscillator frequency on temperature. In contrast, prior time-domain sensors encode sensor information within the time interval of a pulse-position modulation (PPM) or pulse-width modulation (PWM) signal to remove quantization at the sensor, but still retain significant portions of a single-slope ADC to perform explicit voltage-to-time conversion using a continuous-time comparator, which significantly reduces sensor power efficiency [22], [23]. The proposed sensor operates directly from a variable supply voltage, without on-sensor voltage regulation, to eliminate the conversion loss associated with converting harvested energy to a regulated supply. Instead of compensating for supply voltage fluctuations locally, these variations are inherently encoded in the timing characteristics of the transmitted IR-UWB signal and are de-embedded at the receiver through machine learning (ML). Specifically, the ML model exploits a multi-dimensional feature space formed by the intra- and inter-time intervals of the IR-UWB ID to accurately predict temperature while remaining robust to supply voltage variations. Consequently, the sense-transmit architecture can produce significant power reduction, resulting in a sub-20-nW wireless temperature sensor.

II. Proposed ML-Assisted IR-UWB Temperature Sensor

To address the power constraints and variable output voltage of energy harvesters, the proposed sensor is designed to minimize power consumption while operating with a variable supply voltage. Utilizing the sense-transmit architecture, the key objectives are to transmit sensor information without requiring explicit data conversion at the sensor and to minimize the amount of transmitted information while operating with an unregulated voltage supply that would otherwise reduce the power efficiency of the sensor.

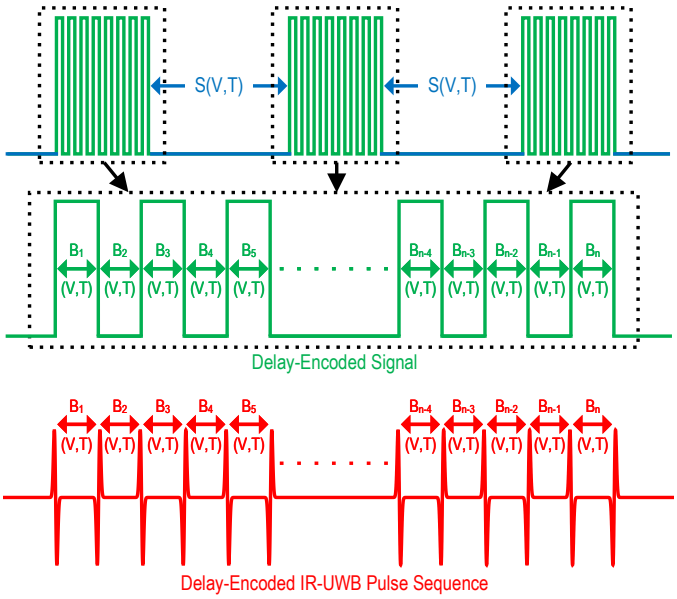


Fig. 1. Core operation of the proposed delay-encoded IR-UWB temperature sensor. Temperature is encoded within all time intervals of the transmission.

A. Principle of Operation

The proposed sensor leverages the inherent temperature dependence of oscillation-based sensors by encoding temperature directly into the delays. The core operation is based on a single oscillator comprised of two temperature-dependent delay lines: one defines the sensor's ID period, S, and the other defines the delay between the bits that form the sensor ID, B_i, generating the delay-encoded signal as illustrated in Fig. 1. The resulting delay-encoded signal is then converted into an IR-UWB signal by transforming each signal edge into a UWB pulse.

Prior work has demonstrated the advantages of encoding sensor information in the time domain to reduce data transmission overhead and the high power consumption associated with ADCs. The architecture in [22] reduces transmitted data by converting a sensed voltage to the time interval between two UWB pulses in a PPM signal using a single-slope voltage-to-time converter (VTC). Although digital conversion is removed, the single-slope VTC still retain significant power overhead due to the continuous-time comparator, high-impedance current sources, references, and switching circuitry, which reduce the sensor's power efficiency [22], [23]. Moreover, the transmission reliability is compromised because the system lacks a method to uniquely distinguish between the two UWB pulses and detect missing pulses. [23] adapts this by replacing the single starting and ending pulses with distinct starting and ending pulse sequences to improve transmission integrity. However, the added robustness reduces or perhaps

removes the data-reduction advantage of the PPM signal in [22]. Encoding a single sensed value with two pulse sequences can increase the number of transmitted pulses when the digital representation of the sensor data requires fewer bits than the pulse sequences, which is significant when power consumption is correlated with the number of transmitted bits. The proposed design removes the distinction between a starting and ending pulse or pulse sequence, reducing the transmitted data by up to 50% compared to [23]. A single pulse sequence conveys temperature information, identification, error detection, and synchronization without transmitting any data bits, thereby achieving the reduced transmission in [22] with the improved transmission integrity in [23].

Instead of deriving temperature from the oscillator frequency, the proposed sensor extracts temperature from the individual delay cells that set B_i. The delay-temperature characteristic arises primarily from variations in carrier mobility (μ) and threshold voltage (V_{th}) with temperature, modelled respectively as

$$\mu(T) = \mu_0 \left(\frac{T}{T_0}\right)^{-m}, \tag{1}$$

$$V_{th}(T) = V_{th}(T_0) - \kappa(T - T_0), \tag{2}$$

where μ_0 is the reference mobility, T_0 is the reference temperature, m is the scattering parameter, T is the absolute temperature, $V_{th}(T_0)$ is the threshold voltage at the reference temperature T_0 and κ is the threshold voltage temperature coefficient. These variations change the propagation delay of the delay cell, allowing temperature to be directly embedded in the transmission delays between each bit, B_i, without explicit data conversion. This sensitivity is further augmented by S, which can be designed to exhibit an exponential temperature dependence to increase the temperature-to-delay conversion gain and improve the overall temperature resolution.

While the delay lines exhibit a temperature dependence that allows temperature to be encoded in the delays, their intrinsic variability also makes them susceptible to changes in the supply voltage. As a result, B_i and S become functions of voltage and temperature (VT), making accurate temperature predictions difficult in the presence of supply variations. This is especially true when powered by an RFEH. The RFEH produces a variable supply voltage due to changing environmental conditions. These variations are typically regulated by a power management unit (PMU) that produces a constant supply voltage regardless of changes in environmental conditions. PMUs can also provide multiple voltage domains to optimize power consumption across different subsystems, or dynamically adjust their output depending on the available power [19]. However, the integration of power management circuits incurs significant power overhead when providing microwatt- or nanowatt-level power, and their quiescent current reduces the output load on the energy harvester, further reducing the available power [22].

B. ML-Assisted Voltage Cancellation

Alternative solutions to mitigate supply voltage variations are needed due to the power constraints imposed by the inefficient PMU voltage regulation for RFEH-powered devices. The proposed design addresses this by shifting supply-variation mitigation from the transmitter to the receiver. The proposed design applies an ML algorithm that computationally cancels the effect of supply voltage variations on the VT-dependent transmission at the receiver rather than actively regulating the supply voltage at the transmitter. This technique allows the sensor to operate across a wide, unregulated supply voltage range, thereby eliminating the need for a PMU and significantly reducing overall circuit complexity and power overhead.

Accurate temperature prediction over a wide voltage range is difficult because a single delay measurement can correspond to a wide range of temperatures due to supply voltage variations. By introducing multiple unique delay responses under the same voltage and temperature conditions, the range of temperatures that would produce the unique combinations of delay outputs is significantly reduced. Increasing the number of distinct delay responses increases the uniqueness of the set of delays, thereby reducing the range of temperatures that would result in the combination of the multiple delays, and increasing the confidence and accuracy of temperature prediction. The proposed system extracts multiple distinct delay measurements from the transmitted signal to create a multi-dimensional delay feature space that can be used to uniquely identify the operating conditions of the sensor.

The distinct delays are due to differences in the underlying delay elements. Within the bit delay line, the odd and even B_i correspond to rising and falling propagation delays, respectively. These exhibit different VT dependencies because μ and V_{th} differ between NMOS- and PMOS-dominated transitions. In addition, intra-die mismatch between delay cells introduces small variations in the VT response among the individual B_i, further increasing the dimensionality of the delay feature space. S, generated by the ID delay line, can be designed to exhibit an exponential temperature dependence as mentioned, which also increases the dimensionality and uniqueness of the delay feature space.

The transmitted IR-UWB ID therefore encodes multiple delays, each with its own distinct VT dependencies. Since each delay responds differently to temperature and voltage, every VT combination can produce a distinct set of delays, therefore, these delays can be used to predict temperature even though the supply voltage is unknown. ML can map the unique delay feature space and learn the relationship between the delays and temperature to distinguish temperature-dependent changes from voltage-dependent changes. A Gaussian process regression (GPR) ML model is used here to jointly interpret these delays to cancel the influence of supply-voltage variation and predict a precise temperature measurement that remains accurate over a wide range of supply voltages. GPR is a non-parametric Bayesian regression method that predicts an unknown output without assuming a fixed functional relationship between the inputs and outputs [24]. It assumes that similar inputs (delays) produce similar outputs (temperatures), with this similarity defined by the kernel function. Given the training delays, the kernel function is evaluated between all training delays to ultimately derive an observation precision

matrix. This matrix describes the direct conditional dependencies among the training delays. Measurement uncertainties are incorporated by modifying the observation precision matrix through a noise variance. For a new test IR-UWB ID, the kernel computes the similarity between the test delays and each training delays in a cross-covariance vector. The model combines these similarities with the training temperatures to produce a predicted temperature as shown:

$$\mu_T = k_*^\top (\mathbf{K} + \sigma_n^2 \mathbf{I})^{-1} T_{tr}, \tag{3}$$

where $k_*^\top$ is the cross-covariance vector between the test delays and training delays, $(\mathbf{K} + \sigma_n^2 \mathbf{I})^{-1}$ is the observation precision matrix with the included noise variance, σ_n^2, multiplied by the identity matrix, $\mathbf{I}$, and T_{tr} and μ_T are the training temperature vector and predicted temperature, respectively. In effect, the prediction is obtained as a weighted combination of the training temperatures, where the weights are defined by the similarity between the new delays and training delays and the conditional dependencies among training delays in the presence of noise. The effects of voltage variation are embedded in the training data and incorporated into the precision matrix through the kernel function, allowing temperature to be inferred from the delays without explicit knowledge of voltage.

From another perspective, the predicted temperature is the expected value of the distribution of the test temperature (T_*) given the training delay data ($\mathbf{X}$), training temperatures and test input (x_*):

$$\begin{aligned}
\mu_T = & \int T_* \Bigg[\iint p(T_* \mid \mathbf{X}, V, T_{tr}, x_*, V_*) \\
& \qquad p(V, V_* \mid \mathbf{X}, T_{tr}, x_*)\, dV\, dV_* \Bigg]\, dT_*, \\
= & \int T_* \Bigg[\iint p(T_*, V, V_* \mid \mathbf{X}, T_{tr}, x_*)\, dV\, dV_* \Bigg]\, dT_*, \\
= & \int T_*\ p(T_* \mid \mathbf{X}, T_{tr}, x_*)\, dT_*,
\end{aligned} \tag{4}$$

where V and V_* are the voltage vectors of the training data and test data, respectively. Taking the integral of the joint probability $p(T_*, V, V_* \mid \mathbf{X}, T_{tr}, x_*)$ gives the marginal probability $p(T_* \mid \mathbf{X}, T_{tr}, x_*)$. As shown, the marginalization removes the need for voltage as an input, therefore, GPR evaluates this marginal probability directly from the delays and training temperatures, without the supply voltage or a physical model that separates the contributions of temperature and voltage. Since this distribution is a weighted average over possible voltages, the smaller the range of possible voltages for a given set of delays, the narrower the distribution and the more certain the prediction. As noted, the transmitted IR-UWB ID narrows the range of possible voltages through multiple delays with distinct VT dependencies to enable an accurate prediction of temperature.

The GPR models are constructed using the process outlined in Fig. 2. To construct a GPR model for temperature prediction, the sensor first undergoes calibration to remove the effects of process variations for a VT mapping of the wireless temperature sensor. To determine the number of calibration

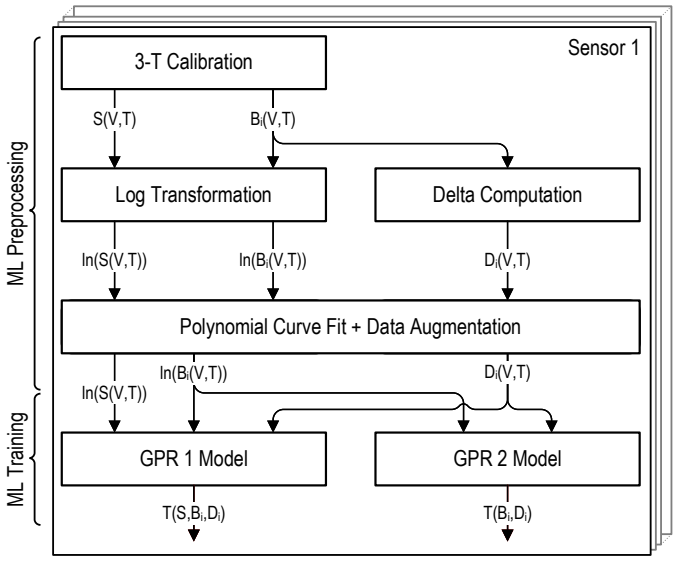


Fig. 2. Construction of the GPR 1 and 2 temperature prediction models with data pre-processing using B_i and S.

temperatures, the general delay responses of B_i and S are evaluated. The delays B_i and S can be derived from the I-V differential equation for a capacitor, $I = CdV/dt$. Under a sharp input step response, B_i can be calculated by recognizing that the PMOS and NMOS spend most of their transition time in the saturation and linear regions. The delay-temperature dependence can therefore be determined by using the I-V equations of the MOSFET in these regions, with μ and V_{th} being the dominant temperature-dependent parameters. Including these temperature dependencies and integrating the differential equation of the capacitor over the linear and saturation regions, the delay of the bit delay cell is given by:

$$\begin{aligned}
B_i = & K_1 T^m \Bigg[\frac{2V_{th}(T)}{(V_{DD} - V_{th}(T))^2} \\
& + \frac{1}{(V_{DD} - V_{th}(T))} ln\left(3 - \frac{4V_{th}(T)}{V_{DD}}\right) \Bigg], \\
ln(B_i) = & ln(K_1) + m ln(T) + ln\Bigg[\frac{2V_{th}(T)}{(V_{DD} - V_{th}(T))^2} \\
& + \frac{1}{(V_{DD} - V_{th}(T))} ln\left(3 - \frac{4V_{th}(T)}{V_{DD}}\right) \Bigg],
\end{aligned} \tag{5}$$

where K_1 represents the temperature-independent terms. At low voltages, B_i depends strongly on both $V_{DD} - V_{th}(T)$ and T^m. While B_i increase with T^m, with m typically equal to 1.5, it decreases with $V_{DD} - V_{th}(T)$. Depending on the value of the overdrive voltage, $V_{DD} - V_{th}(T)$, the temperature dependence of V_{th} may cancel out with μ, creating a temperature-insensitive delay. However, for sufficiently large overdrive voltages, the sensitivity to the overdrive voltage decreases, allowing mobility temperature effects to dominate. This causes an increasing B_i with temperature as mobility decreases with T^{-m}, with a slight curvature as the current increases slightly with a decreasing V_{th}. The difference in mobility and threshold voltage between the PMOS and NMOS transistors results in slightly different rising and falling edge

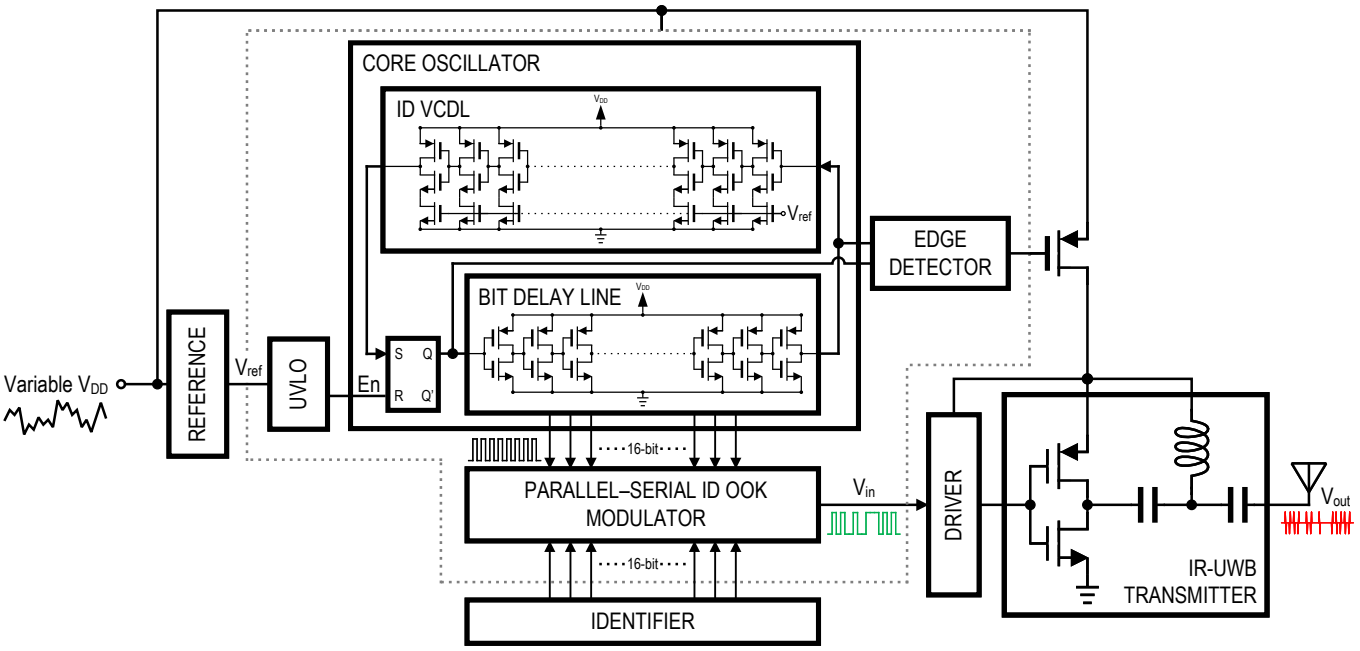


Fig. 3. Circuit implementation of the proposed delay-encoded IR-UWB temperature sensor.

delays.

S can be implemented with an exponential temperature dependence by controlling the delay with the subthreshold current of a footer transistor for higher sensitivity to temperature, as will be discussed in Section II-C:

$$\begin{aligned} S &= K_2 V_{DD} T^{m-2} exp\left(-\frac{V_{ref}-V_{th}}{nV_T}\right), \\ ln(S) &= ln(K_2) + ln(V_{DD}) + (m-2)ln(T) \\ &\quad - \left(\frac{V_{ref}-V_{th}}{nV_T}\right), \\ &= ln(K_2) + ln(V_{DD}) + (m-2)ln(T) \\ &\quad - \left(\frac{q(V_{ref}-V_{th}(T_0)-\kappa T_0)}{nkT}\right), \end{aligned} \tag{6}$$

where K_2 represent the temperature-independent terms of S, V_T (kT/q) is the thermal voltage and n is the subthreshold slope factor. The inherent non-linearities in the delay responses of B_i and S in the form of the power, inverse power and exponential terms can be reduced through log transformation and Taylor series approximation. Taking the logarithm of B_i in (5) turns the multiplicative terms into additive terms. This transformation dampens the effects of higher-order terms and reduces the curvature of the B_i. Within a bounded temperature range, the log-transformed B_i can be approximated by a second-order Taylor polynomial derived from (5), with the form $f(T_0) + f'(T_0)(T-T_0) + f''(T_0)(T-T_0)^2/2$, while preserving the delay variations caused by the difference in temperature effects between μ and V_{th}. While the polynomial approximation is not exact, its adaptability allows for non-idealities such as mobility degradation, velocity saturation and drain-induced barrier lowering (DIBL) to be accounted for in the curve fit. Similarly, applying a log transformation to (6) linearizes the exponential and transforms (6) to a multiple linear regression model that can likewise be approximated by a second-order Taylor polynomial. Since the transformed delay responses can be characterized by a second-order polynomial or multiple regression model with two independent variables, a three-temperature calibration evaluating the delay response over voltage can model both B_i and S. The difference between two consecutive B_i (D_i = B_i-B_{i+1}) is calculated to exploit differences in rising and falling edge delays, to further increase the dimensionality of the delay feature space. The three-temperature calibration data is then augmented over voltage and temperature to provide more data. Using the delay feature space, two GPR models are trained to predict temperature: one utilizing B_i and D_i, and another utilizing B_i, D_i and S to improve prediction.

An alternative joint-sensor approach for measuring temperature over a 0.4 V range was proposed in [25]. This design utilizes a separate voltage sensor to compensate for the temperature sensor's slight voltage dependency using a least-squares method. However, this approach requires two separate sub-sensors and two separate two-step least-squares models for each sub-sensor. The initial models require a high-VT resolution multi-sensor calibration followed by individual sensor calibrations, resulting in a total of four calibrations per temperature sensor. Furthermore, the voltage sensor is created by the mutual compensation between mobility and threshold voltage [26], which limits voltage scalability.

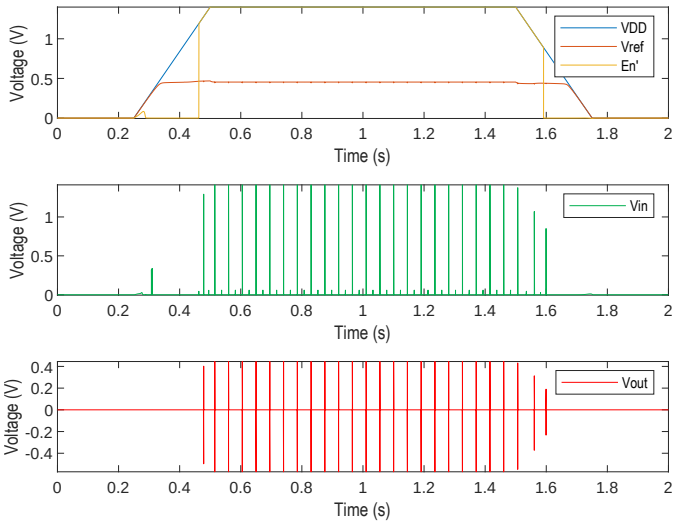
C. Circuit Implementation

The sensor's circuit implementation is shown in Fig. 3. The bit delay line produces a 16-bit parallel output that feeds the transmitter and sets B_i using high-threshold-voltage transistors to reduce leakage in inverter-based delay cells for transmission at a nominal pulse repetition rate (PRF) of approximately 10 MHz. The sensor nominally transmits an IR-UWB ID every

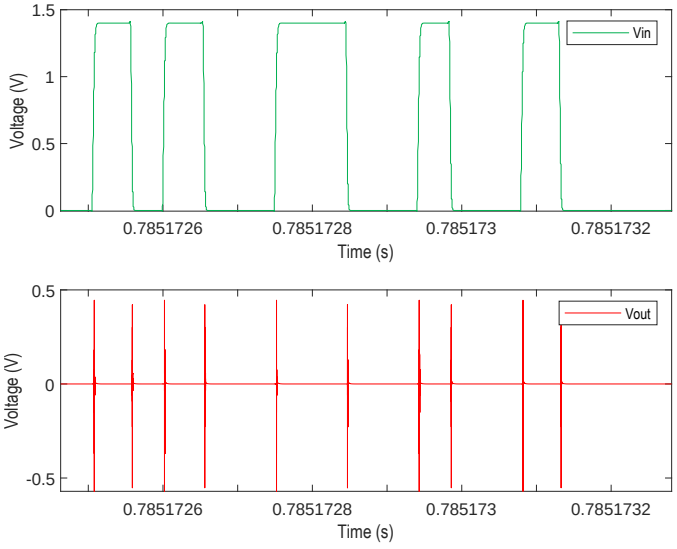
50 ms as set by the ID delay line. Since ambient temperature changes slowly, higher sampling rates are unnecessary for detecting environmental temperature changes. The ID period displays an exponential temperature response by current starving the falling transition of the delay cells through footer transistors and V_{ref} to operate under subthreshold conditions in a voltage-controlled delay line (VCDL). Current starving the inverter creates a low-power, high-temperature-sensitivity delay. The delay of the falling transition is significantly greater than that of the rising transition, making the rising transition's delay negligible. This also reduces the circuit required to implement a current-starved rising transition and accompanying reference voltage for the header transistor. The core oscillator, which contains the ID VCDL and bit delay line, enables the encoding of temperature within the transmission intervals and simultaneously drives the transmitter, eliminating the dedicated comparators, high-impedance current sources, references and control circuitry required for the VTC in prior works. While sensitive to jitter, noise and variations in PVT conditions, the free-running ring oscillator consumes the least power compared to relaxation or LC oscillators. The bit delay line produces a pulse train modulated by on-off keying (OOK) using the system's binary ID, via a parallel-serial ID OOK modulator composed of NAND, NOR, and XNOR gates with thick-oxide transistors. The relatively fast switching speed of the parallel-serial ID OOK modulator has a limited effect on B_i, thereby maintaining the temperature encoding of the bit delay line.

The ID uniquely identifies the sensor. The proposed design implements an impulse-based UWB transmitter that consists of a driver, a digital switch-mode power amplifier and a pulse-shaping filter, as shown in Fig. 3. IR-UWB transmits ultra-short-duration wideband pulses, in contrast to a modulated continuous carrier signal, which drastically reduces power consumption by eliminating the need for continuous transmission. The short-duration pulse-based transmission is inherently resilient to multipath propagation and interference. As a result, IR-UWB pulse transmission reduces power consumption, improves power efficiency, and enhances transmission reliability. The OOK-modulated ID signal is passed through a driver that is increasingly sized towards the output to optimize the rise and fall times, and through an edge-based switch-mode power amplifier that shapes the signal into positive and negative Gaussian monocycle pulses, using a T-network pulse-shaping filter centered around 6 GHz. Power to the transmitter is gated through the core oscillator and edge detector to limit the leakage. By representing the ID as a series of pulses, only a digital input bit sequence is required for transmission. This enables direct integration of the digital ID VCDL and bit delay line with the transmitter without requiring explicit data conversion, removing the need for ADCs and DACs in the sense-transmit architecture. Aside from the voltage reference and pulse-shaping filter, the entire system is implemented digitally, which significantly reduces power consumption.

Fig. 4 demonstrates the modulation of the pulse train from the delay line to produce a 16-bit OOK-modulated IR-UWB ID. The shown pulse sequence contains 3 synchronous bits at the beginning, which also serve as a start marker for the



(a)



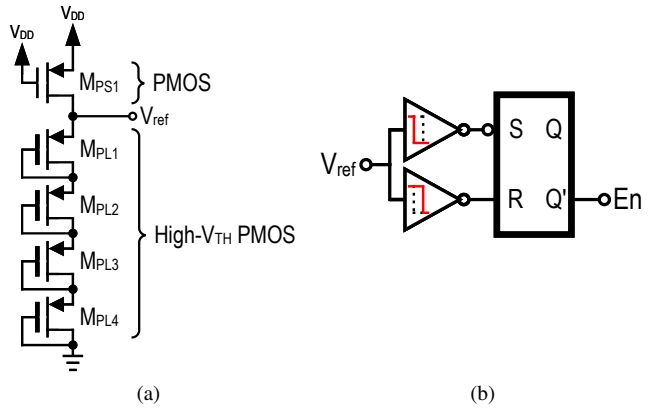
(b)

Fig. 4. (a) Simulated operation of the proposed IR-UWB temperature sensor, including start-up and shut-down and output of the sensor. (b) Detailed view of the OOK-modulated bit stream and transmission output of the IR-UWB ID in Table I.

TABLE I
IR-UWB ID EXAMPLE FOR SYNCHRONIZATION, IDENTIFICATION AND ERROR DETECTION FOR THE IR-UWB TEMPERATURE SENSOR.

Start Sync.			8-bit Unique Identifier								5-bit CRC				
1	1	1	1	0	1	0	1	0	1	1	0	1	1	0	0

transmitted sequence. Between the synchronous bits are the 8 identifier bits, unique to the sensor. While the IR-UWB pulse sequence intrinsically provides a parity error check through its alternating sequence of positive and negative Gaussian monopulses, the pulse sequence can include a 5-bit cyclic redundancy check (CRC) for improved error detection. An example of the IR-UWB ID is shown in Table I, with the 5-bit CRC produced using the polynomial $x^5 + x^3 + 1$, which creates the digital sequence from the OOK-modulator in Fig. 4(b). A rising or falling transition represents a binary one,



(a) (b)

Fig. 5. Schematic of the (a) PMOS-only voltage reference and (b) digital UVLO.

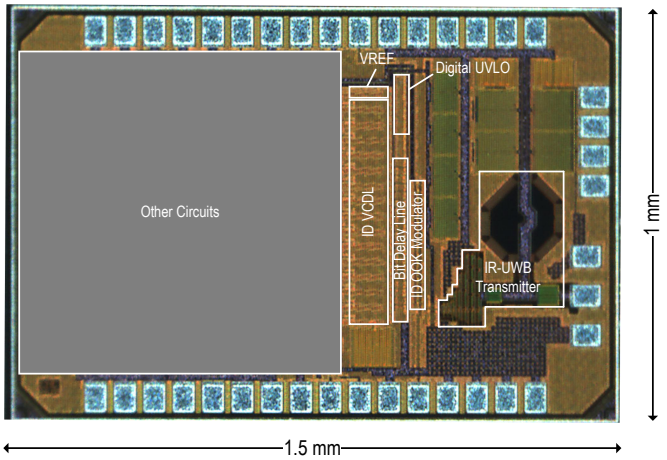


Fig. 6. Image of fabricated IR-UWB temperature sensor.

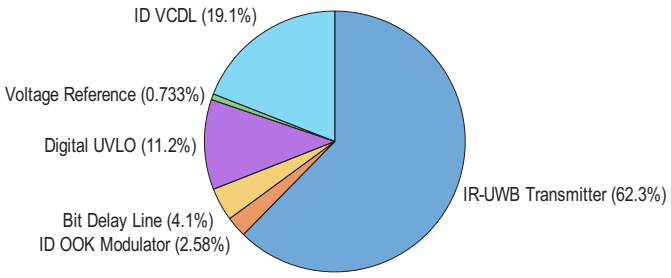


Fig. 7. Power consumption breakdown across major subsystems of the proposed IR-UWB temperature sensor.

while an unchanged state/constant state represents a binary zero. This is transformed into a UWB pulse sequence through the edge-based switch-mode power amplifier. This ensures the robustness of the transmission.

The sensor is enabled by an undervoltage lockout (UVLO) circuit that utilizes a voltage reference, shown in Fig. 5(a), based on [27], which also provides V_{ref} for the ID VCDL. The native NMOS transistor that serves as a current source in [27] is replaced with a PMOS transistor, and the output reference voltage is determined by the threshold voltage of the four high-threshold-voltage PMOS transistors that act as the load. The exclusive use of PMOS transistors in the design reduces the process variations of the voltage reference. This turns on the sensor when sufficient energy is stored in the energy harvester to transmit multiple temperature readings. Without sufficient power, the sensor is disabled to minimize power consumption and allow energy to be accumulated through an energy harvester. Conventional comparator-based UVLOs draw a constant static current, increasing the sensor's power consumption. We present a digital UVLO circuit that eliminates the continuous current draw associated with comparator-based UVLOs. The structure of the proposed digital UVLO circuit is shown in Fig. 5(b) and features only two skewed inverters connected to an SR-latch. The top and bottom inverters are skewed for high- and low-voltage transitions, respectively, to introduce hysteresis through the SR-latch to enable the sensor at 1.2 V and disable it below 1 V. This prevents the system from repeatedly toggling between enable and standby states during start-up, which could occur due to slight voltage drops caused by the system's instantaneous current draw. The start-up SR-latch allows the system to complete transmitting the last ID, ensuring the sensor operates reliably. The operation of the UVLO circuit and voltage reference is demonstrated in Fig. 4(a).

III. Results and Evaluation

The proposed IR-UWB temperature sensor was implemented and fabricated in TSMC's 130 nm CMOS process and occupies an active area of 0.16 mm^2, including the pulse-shaping filter. Fig. 6 shows the fabricated sensor with the major subsystems highlighted. The sensor's power consumption was found to be 16.7 nW at 1 V VDD and 30°C while transmitting all 16 pulses in the IR-UWB ID. High-voltage 3 V transistors were used throughout the design to minimize power leakage. Fig. 7 presents a power breakdown of the major subsystems of the sensor. The core of the sensor accounts for 23% of the total power. With explicit data conversion, voltage regulation, and typical clock generation removed, and temperature and voltage encoded directly within the transmission intervals, the IR-UWB transmitter accounts for the majority of the system's power consumption, resulting in higher transmission efficiency.

Fig. 8 shows the experimental setup used to evaluate the sensor. The sensor is mounted on a PCB to provide power and is probed using a Z40-X-GSG-100 probe on a Cascade Microtech probe station connected to a Keysight UXR11102B oscilloscope sampling at up to 256 GS/s. While the sensor was simulated to operate at sub-zero temperatures, its performance was experimentally characterized from 10°C to 110°C due to vertical space constraints on the probe station. The sensor's temperature was varied using a thin-film polyimide heater above room temperature, while a thin thermoelectric cooler was used to cool the sensor for measurements at 10°C. The sensor was measured at five temperatures, with the supply voltage varied from 1 V to 3 V at each temperature. Two PT1000 Class A reference temperature sensors were placed in

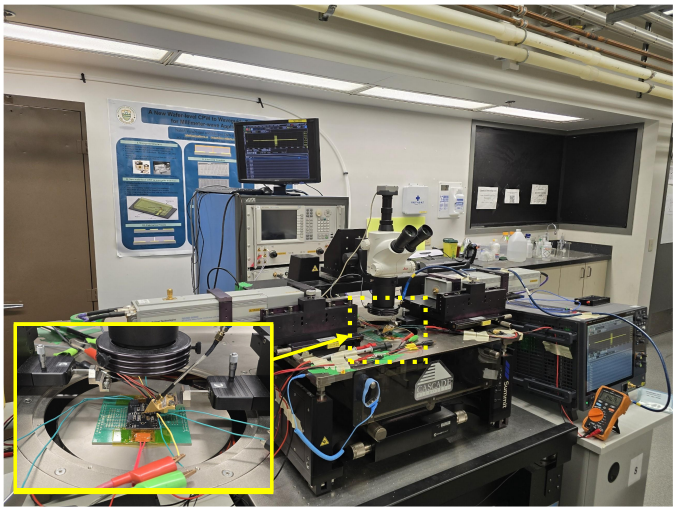


Fig. 8. Experimental setup for evaluating the proposed IR-UWB temperature sensor on an RF probe station showing the polyimide heater attached to the test PCB.

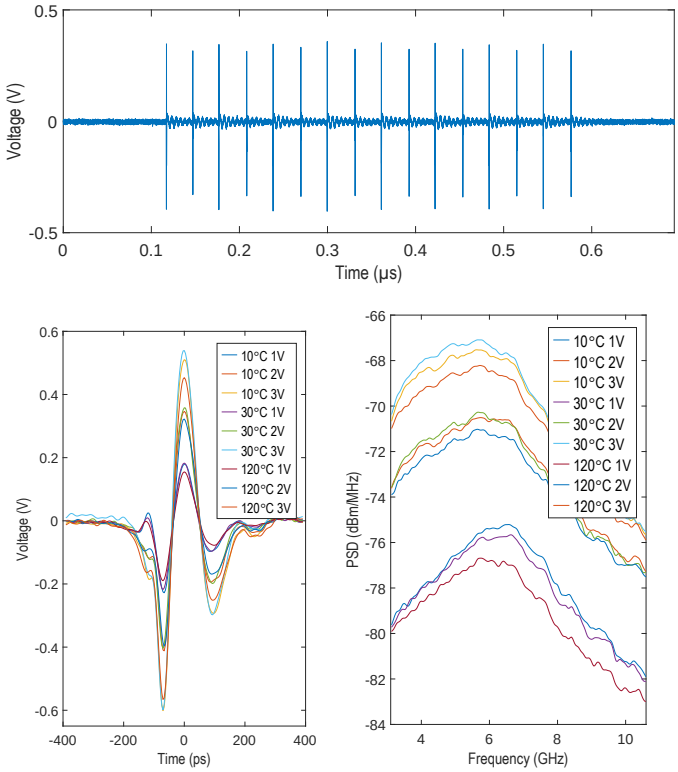


Fig. 9. (a) Measured transient response of the 16-bit IR-UWB output, (b) peak-to-peak voltage and shape of the rising-edge IR-UWB pulses and (c) the PSD of the IR-UWB transmission under different operating conditions.

close proximity to the proposed sensor to provide a reference temperature reading. A total of six sensors on separate dies were characterized.

The IR-UWB output of the sensor was captured by the oscilloscope for time- and frequency-domain analysis and characterization of the sensor's performance. Fig. 9(a) shows an example of the transient response of the measured 16-pulse IR-UWB ID. The pulse shape and peak-to-peak voltages (V_{pp}) across different operating conditions of the sensor are shown in Fig. 9, along with their power spectral density. The V_{pp} ranges from a minimum of 0.34 V to 1.14 V. The potentially high peak-to-peak pulse amplitude improves the transmission range. Despite this, the signal's PSD remains below the FCC UWB spectral mask of –41.3 dBm/MHz across all operating conditions, as the low pulse-repetition rate and the reduced transmission from delay encoding limit the average radiated power.

Peak detection is applied to the sampled IR-UWB signal to determine the time intervals between and within the transmission. B_i and S were determined from the IR-UWB signal across hundreds of IR-UWB IDs at each measured voltage and temperature. Using all the measured data, B_i and S were further interpolated to provide data at 5°C and 0.05 V increments. The ML construction process, depicted in Fig. 2, is applied to this high-resolution dataset. The sensors were calibrated at 20°C, 60°C and 105°C for the GPR 1 model, and 15°C, 60°C and 105°C for the GPR 2 model across the operating voltage range. The calibration can account for variations in V_{ref} as well as potential supply voltage droop during operation due to instantaneous current draw. Process variation in V_{ref} is absorbed into the sensor's VT mapping during calibration, since the mapping is extracted from each sensor's measured response. Supply voltage droop that occurs without a sufficiently sized supply capacitor is deterministic and appears as a decrease in delay within the IR-UWB ID that can also be captured in the VT mapping. From the calibration datasets, the first two B_i values and S values were extracted for the GPR 1 model, while the first and last five B_i delays were extracted for the GPR 2 model. The parameters B_i and S are log-linearized, and D_i is computed from B_i. B_i, S and D_i are augmented a resolution of 5°C and 0.05 V using the polynomial curve fits. GPR models are trained and tested on the augmented measurement data to assess model accuracy.

Fig. 10 illustrates the resulting temperature accuracy of the two temperature prediction models. It shows the simulated residual errors across the five process corners overlaid on top of the measured residual errors of the proposed temperature sensor across six sensors on six distinct dies, evaluated over all temperature and voltages. Using only B_i, the GPR 2 model achieves a measured inaccuracy of $\pm$0.69°C (σ) and a mean absolute error (MAE) of 0.39°C across the full operating range, as shown in Fig. 10(b). A performance deviation between measurement and simulation is observed with the GPR 2 model. This is due to differences observed between the simulated and measured B_i values, where the measured B_i exhibits much lower linearity, much higher mobility degradation and more significant velocity saturation than found in simulation. Additionally, temperature prediction using the GPR 2 model degrades at lower voltages. At 1 V, B_i becomes temperature-insensitive due to the mutual compensation between mobility and threshold voltage [26], creating a zero-temperature-coefficient (ZTC) point. Compounded with slight measurement inaccuracies and variations, this ZTC point exhibits the largest residual errors.

The accuracy of the sensor using the GPR 2 model can be improved by increasing the minimum operating voltage to avoid the ZTC point in B_i. Operating within a reduced voltage

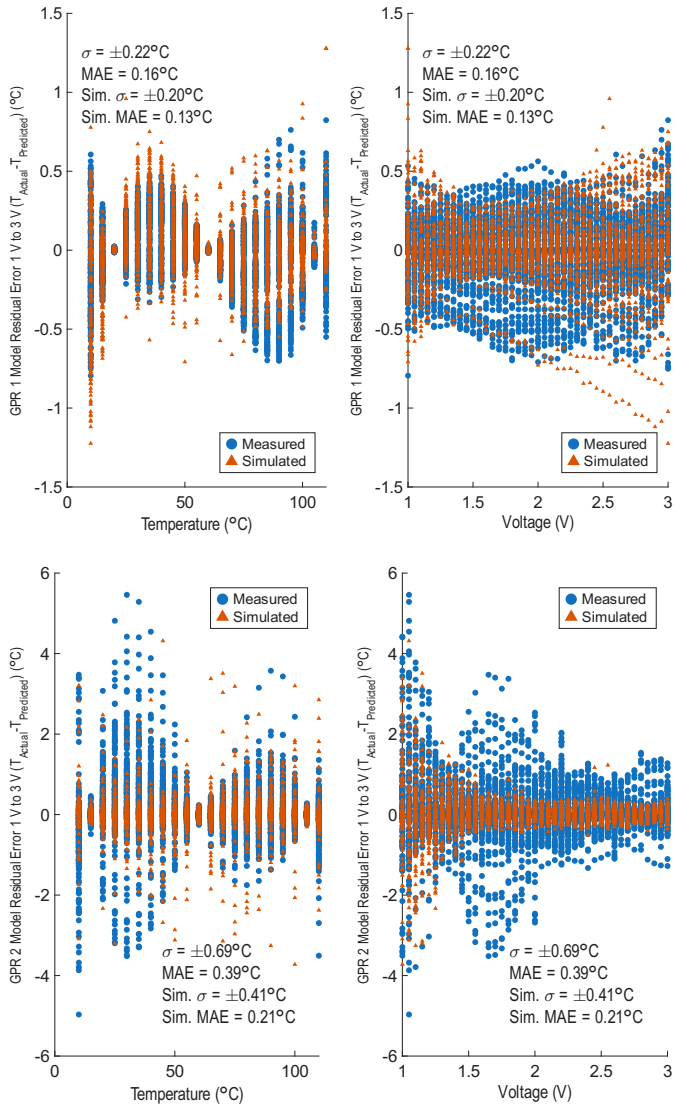


Fig. 10. Performance of the temperature sensor measured across six sensors and simulated across the five process corners over its full voltage range of 1 V to 3 V, evaluated over temperature and voltage using the (a) GPR 1 Model with S, B_i and D_i, and (b) GPR 2 Model with B_i and D_i.

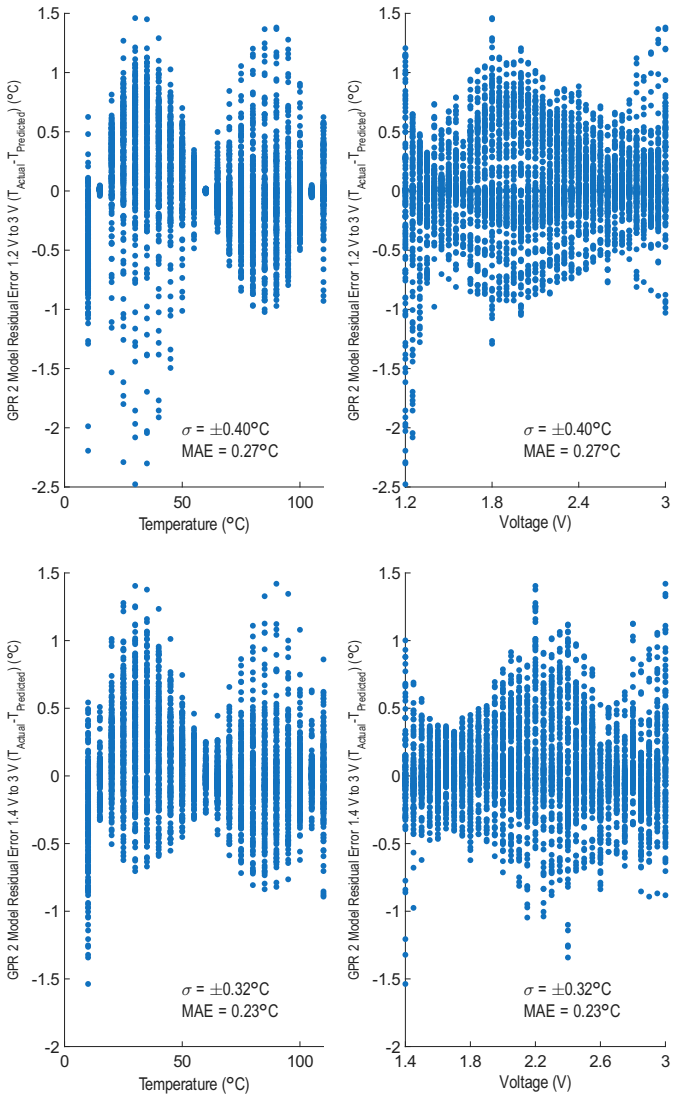


Fig. 11. Measured performance of the temperature sensor across six sensors, evaluated over temperature and voltage using the GPR 2 Model with B_i and D_i over a reduced voltage range: (a) 1.2 V to 3 V and (b) 1.4 V to 3 V.

range of 1.2 V to 3 V significantly reduces the inaccuracy to ±0.40°C (σ) and 0.27°C (MAE), as shown in Fig. 11. Further increasing the minimum operating voltage to 1.4 V reduces the σ and MAE to ±0.32°C and 0.23°C, respectively.

To achieve high temperature accuracy while operating at low supply voltages, the GPR 1 model can be used. Because S maintains an exponential temperature dependency across all voltages, it avoids the ZTC point found in B_i. As shown in Fig. 10(a), the measured σ and MAE are slightly higher for the GPR 1 model than the simulated errors, which is attributed to measurement errors that affect the smoothness of the experimental delay VT response, arising from slight deviations between the reference and actual temperatures in the unenclosed testing environment. Despite this, the proposed temperature sensor displays the best performance with the inclusion of S using the GPR 1 model, achieving a measured σ and MAE of ±0.22°C and 0.16°C across all temperatures, voltages, and sensors.

The performance of the GPR 1 model can be further improved by applying a systematic error correction [17]. Residual errors in calibration primarily stem from higher-order temperature variations, which, while subject to process variations, are deterministic. This can be mitigated by applying a fixed systematic polynomial correction to B_i and S. The fixed polynomial is derived from a one-time characterization, using high-resolution measurements averaged across a sample of sensors. Applying this systematic correction to a three-temperature calibration reduces the σ and MAE of the GPR 1 model down to ±0.19°C and 0.13°C. Alternatively, this correction can be applied to reduce the calibration effort. Three-temperature calibrations require significant effort due to the time needed to achieve thermal equilibrium for testing at each calibration temperature. By performing a linear calibration and applying the fixed systematic polynomial correction, obtained by a one-time characterization of the average residual

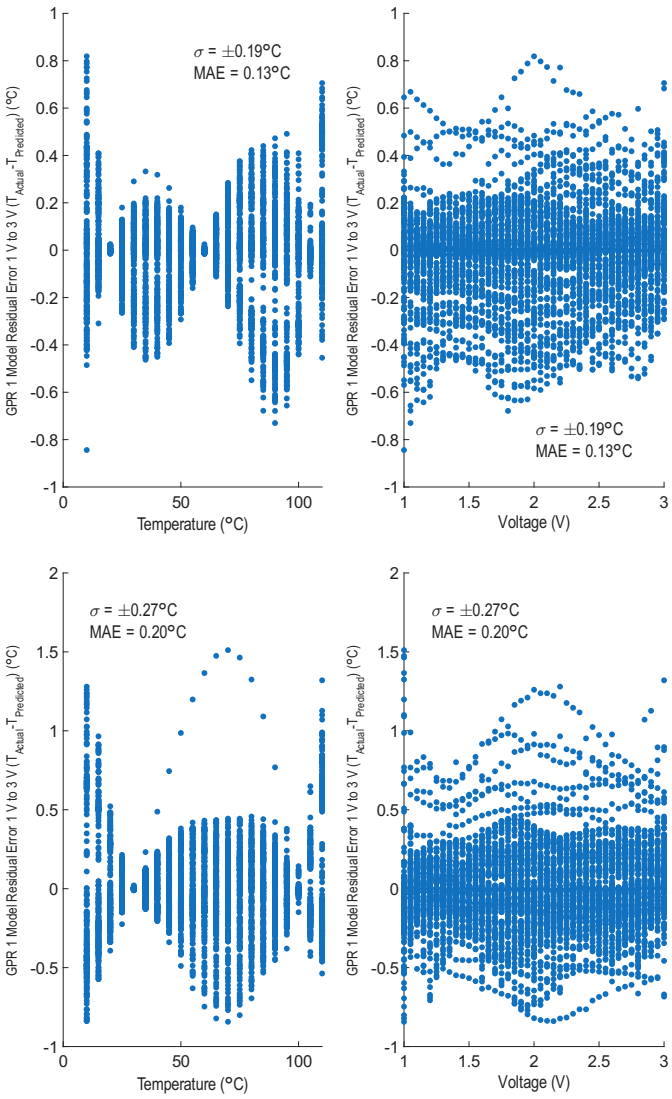


Fig. 12. Measured performance of the temperature sensor across six sensors over its full voltage range of 1 V to 3 V, evaluated over temperature and voltage using the GPR 1 Model with a fixed systematic polynomial correction for (a) three-temperature and (b) two-temperature calibration.

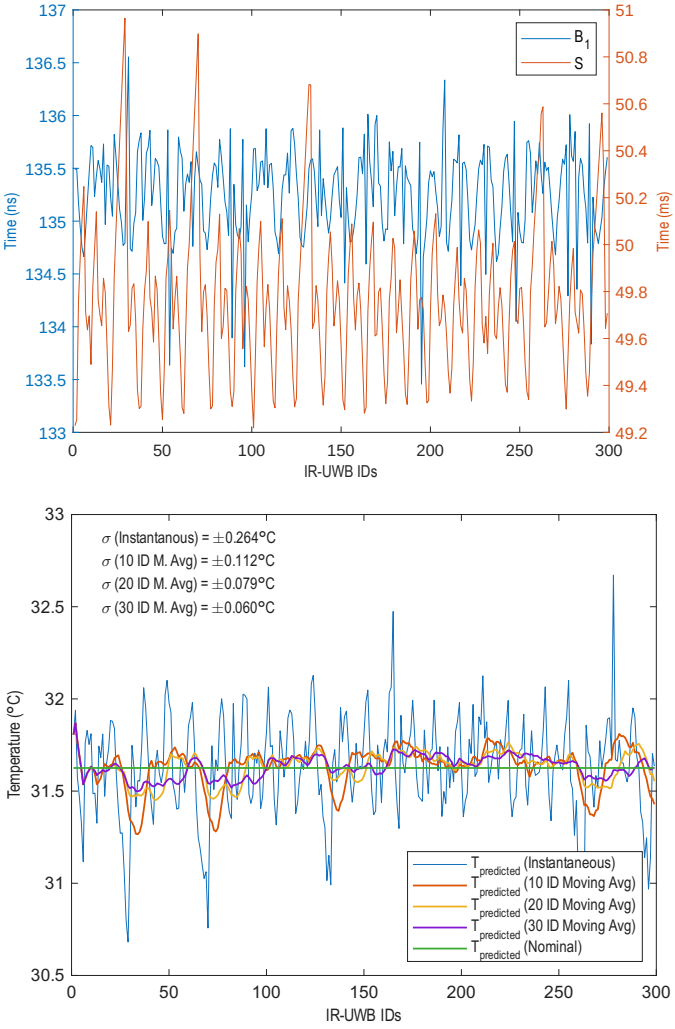


Fig. 13. Effects of measured noise and jitter on (a) S and B_1, and (b) predicted temperature.

error of several sensors, the temperature prediction model can be created with a two-temperature calibration with the performance shown in Fig. 12. This achieves performance close to a three-temperature calibration without the systematic error correction, with a σ and MAE of $\pm$0.27°C and 0.20°C.

While the delay-line-based sensing implemented in the design contributes to the sensor's low overall power consumption by enabling a direct digital implementation with the IR-UWB transmitter that simultaneously senses and transmits with no explicit data conversion, ring oscillators are more sensitive to noise and jitter than their relaxation and LC oscillator counterparts. The GPR models are trained on delay inputs that are assumed to be operating on a supply that is stable or predictable for the duration of the transmission of a single set of delays. However, both low- and high-frequency supply and device noise can result in jitter that affects the delays within a single transmission. Each delay within the delay set may therefore correspond to a slightly different VT combination. Equation (3) can account for some of these variations through the added noise variance. When supply and device noise are high and beyond what is captured in training, averaging can reduce the effects of noise and jitter. The impact of noise and jitter on S and B_i, as represented with B_1, is shown in Fig. 13(a), and its effects on the predicted temperature are also shown in Fig. 13(b) across the measurement of 300 IR-UWB IDs. While noise and jitter can affect the sensor's predicted temperature, resulting in spikes in the predicted temperature, the σ between the nominal predicted temperature and the instantaneous predicted temperature is only $\pm$0.264°C. Averaging can significantly reduce the spikes in the predicted temperature, and σ can be reduced by more than half to $\pm$0.112°C by applying a moving average across 10 IDs and even further with larger moving averages. Therefore, the effects of noise and jitter can be mitigated. This averaging can mitigate delay variations in S and B_i induced by low- and high-frequency supply noise, in conjunction with its attenuation by on-chip and off-chip decoupling capacitors.

The temperature sensor's precision is otherwise limited by the receiver's time resolution. To maximize the temperature

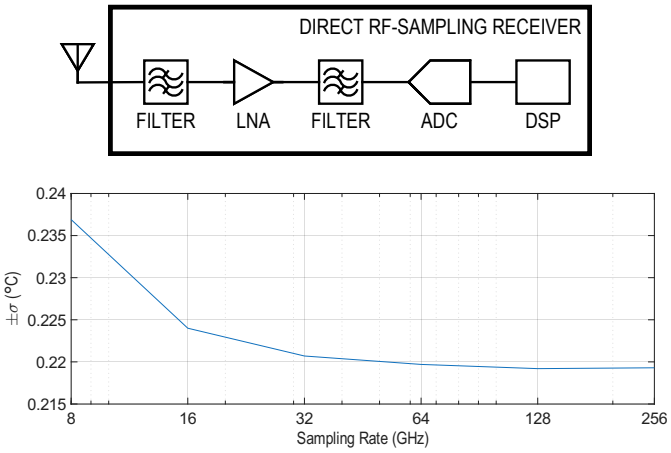


Fig. 14. (a) Example of a receiver for the proposed sensor. (b) Effects of sampling rate on the measured temperature resolution.

resolution, the receiver should distinguish variations in B_i. Reducing the receiver's time resolution may reduce the temperature resolution if B_i cannot be uniquely identified. The effects of the receiver's time resolution on the error of the temperature sensor are analyzed by reducing the sampling rate of the receiver from 256 GS/s down to 8 GS/s, as shown in Fig. 14(b). The reduction in sampling rate shows a minimal change in the achievable temperature resolution. At 4 GS/s, the receiver becomes unable to detect the UWB pulses reliably. Therefore, the minimum time resolution required is determined by the detection of UWB pulses, not by the sensor's temperature resolution. For practical deployment, the oscilloscope used to characterize the performance of the proposed sensor can be replaced by a direct RF-sampling IR-UWB receiver, as illustrated in Fig. 14(a), consisting of a passband filter, low-noise amplifier (LNA), high-speed ADC and digital signal processor (DSP). The high-speed ADC with sampling rates higher than or equal to 8 GS/s directly digitizes the IR-UWB signal. Peak detection can be applied to the digitized RF signal by implementing an energy detection, cross-correlation or auto-correlation receiver in the DSP that transforms the IR-UWB signal to rectangular pulses and extracts the time-of-arrival (ToA) via zero-crossing detection. These ToAs can be converted into delays as inputs to the deployed temperature prediction model at the receiver for inference to predict the sensed temperature at the wireless sensor node.

The communication range between this sensor node and the receiver is determined by the transmitted power of the pulse. At nominal conditions, the 16-bit IR-UWB pulse sequence has a maximum average PSD of -75.66 dBm/MHz as shown in Fig. 9(c). The IR-UWB pulse PSD is calculated by accounting for the duty cycle, which is the product of the pulse width (400 ps) and the PRF (7.5 MHz). This yields a maximum pulse PSD of -50.43 dBm/MHz ($-75.66\text{dBm/MHz} - 10\log_{10}(400\text{ ps} * 7.5\text{ MHz})$). With a -10 dB bandwidth that spans the entire UWB frequency range, the maximum transmitted power is approximately -11.68 dBm [22], which corresponds to a wireless transmission range above 30 m given a typical receiver sensitivity of -90 dBm in free space.

The long-term reliability of the proposed sensor is another consideration. Since the temperature prediction model is trained with an initial calibration, circuit degradation from hot-carrier injection (HCI) and bias-temperature instability (BTI) can reduce sensor accuracy over time. However, due to the low switching activity and low power consumption of the circuit, the sensor is less susceptible to HCI aging effects than its conventional high-power alternatives. Although aging effects were not experimentally evaluated, these mechanisms are deterministic. Consequently, delay drifts may be compensated for within the temperature prediction model by incorporating the operating lifetime as an additional input parameter alongside the delay features. If necessary, periodic recalibrations can also maintain sensor accuracy over time.

Table II summarizes the performance of the proposed IR-

TABLE II
PERFORMANCE SUMMARY AND COMPARISON TO TIME-MODULATED IR-UWB SENSORS.

Ref.	Tech. (nm)	VDD (V)	Area (mm^2)	Cal.	UWB-V_{pp}	Pulses / Conversion	ID length (Bits)	Conv. Time	ENOB (Bits)	Samp. Rate	Power	FoM (pJ/ Conv. Step)
[22]	180	1.2/1.8	2.5[a]	Offline Cal + Online 2 Point Cal	350 mV	2	0	3.3 µs	6.7 (7.3[b])	300 kS/s	41.5 µW	1.3 (0.9[b])
[23]	130	1.2	1.35	3 Point	160 mV	32	6	1 ms	11.3	1 kS/s	70 µW	0.87[c]
This Work	130	1.4 to 3	0.16[d]	3 Temp	400 mV	16	4	2 µs	7.9	20 S/s	16.7 nW	3.5
		1-3				32 (16[e])	13	50 ms	8.4	20 S/s	16.7 nW	2.4
										5.4 kS/s[f]	928 nW[f]	0.5
				3 Temp[g]					8.7	20 S/s	16.7 nW	2
										5.4 kS/s[f]	928 nW[f]	0.4

[a] Active area only [b] Integration window reduced from 10 ns to 2 ns [c] Divided by 32 channels [d] Active area and pulse-shaping filter included
[e] Pulses required for conversion converge to 16 as the number of transmitted IR-UWB IDs approaches infinity [f] Calculated with reduced ID VCDL
[g] With the fixed systematic polynomial correction

TABLE III
PERFORMANCE SUMMARY AND COMPARISON TO STATE-OF-THE-ART WIRELESS SENSORS DESIGNED FOR ENERGY-HARVESTER-POWERED OPERATION.

Reference	This work	[22]	[28]	[29]	[30]	[31]	[32]	[33]
Technology (nm)	130	180	55	180	65 LP	65	180	130
Operating Voltage (V)	1 to 3	1.15 to 1.3	1.8	0.6	0.35	1	2-3.8	0.7-1.2
Area (mm^2)	0.16[a]	2.5[b]	0.56	1.3	0.151[b]	1	2.25	0.23[b]
Sensing Technology	Delay Encoding	PPM	Analog to Digital	Analog to Digital	Analog to Digital	Pulse Encoding	Analog to Digital	Frequency Encoding
Wireless Technology	IR-UWB	IR-UWB	Backscatter	Backscatter	CW	Backscatter	CW + Backscatter	Backscatter
Sampling Rate	20 S/s	300 kS/s	20 S/s	-	20 S/s	-	0.03 S/s	40 S/s
Power	16.7 nW	41.5 µW	25 µW	982 nW[d]	127.5 nW	7.32 µW	143 nW	1.05 µW

[a] Active area and pulse-shaping filter included [b] Active area only [c] Peak power

UWB sensor and compares it with other time-modulated IR-UWB sensors. The proposed IR-UWB sensor achieves an ENOB of 8.4 and 7.9 bits with the GPR 1 and 2 models, respectively, as defined in [22] across a temperature range of 100°C. This increases to 8.7 bits while using the GPR 1 model with a fixed polynomial correction. The nominal sampling rate is intentionally reduced to account for the slow change of ambient temperature, where high sampling rates are unnecessary. Under this condition, the total power consumption is 16.7 nW with a nominal V_{pp} of 400 mV. However, at this low sampling rate, the design becomes leakage-dominant, and power does not scale linearly with sampling rate. By reducing the ID VCDL to a single stage, the sampling rate is calculated to increase to 5.4 kS/s while the power consumption increases to 928 nW. At this operating point, leakage is no longer dominant, and the IR-UWB transmitter accounts for more than 80% of the total power consumption. With the GPR 1 model, this condition yields the highest FoM, as defined in [22] and [23], with and without the fixed polynomial correction, among the compared time-modulated IR-UWB sensors. The strong FoM reported in [22] stems from transmitting only two pulses to represent sensor data using PPM, since active transmission power scales with the number of transmitted pulses. While reducing the number of transmitted pulses improves efficiency, transmitting only two pulses provides no means of sensor identification or error detection and cannot be used in practice. This limitation is addressed in [23] through transmission of two 16-bit pulse sequences, and in this work by transmitting a 16-bit IR-UWB ID. It should be noted that the FoM of [23] is evaluated per channel, allowing auxiliary and conversion power to be distributed across 32 channels that reduces the impact of architectural power inefficiencies. This reduces the apparent power overhead and is only achievable in multi-channel architectures. [23] also has a much lower peak transmit power with a 150 mV_{pp} output. Compared with the other works, this work achieves reliability in operation and sensing while reducing power inefficiencies through the transmitted VT delay-encoded OOK IR-UWB ID and ML-applied voltage cancellation to eliminate data conversion, digitization, and voltage regulation for the lowest power consumption while having the highest peak output power.

Table. III presents a general comparison with other wireless sensors designed for energy-harvester-powered operation. The proposed sensor achieves the lowest power consumption and the widest operating voltage range of the reported works.

IV. CONCLUSION

This work presents an IR-UWB temperature sensor featuring a simultaneous sense-transmit architecture that eliminates the need for explicit on-sensor data conversion and data bit transmission by transmitting a VT delay-encoded IR-UWB ID. An ML algorithm applied at the receiver can predict temperature in the presence of voltage variations to eliminate the need for voltage regulation at the sensor. This sensor architecture significantly reduces power consumption. As a result, the proposed IR-UWB temperature sensor operates with the lowest power and the widest operating voltage range of the reported works. Experimental results demonstrate a temperature prediction inaccuracy of $\pm$0.22°C (σ) and 0.16°C (MAE) across a supply range of 1 V to 3 V, respectively. Applying a fixed systematic polynomial correction reduces the σ and MAE to $\pm$0.19°C and 0.13°C, respectively. With sub-20-nW power consumption and the capability to operate on a wide variable supply voltage, the sensor operates reliably despite the limited and variable output of energy harvesters, making it highly suitable for energy-harvested IoT sensing.

REFERENCES

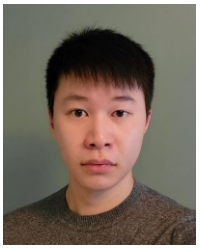
[1] G. Papotto, F. Carrara, and G. Palmisano, "A 90-nm CMOS Threshold-Compensated RF Energy Harvester," *IEEE J. Solid-State Circuits*, vol. 46, no. 9, pp. 1985–1997, 2011.

[2] Z. Hameed and K. Moez, "A 3.2 V –15 dBm Adaptive Threshold-Voltage Compensated RF Energy Harvester in 130 nm CMOS," *IEEE Trans. Circuits Syst. I*, vol. 62, no. 4, pp. 948–956, 2015.

[3] A. S. Almansouri, M. H. Ouda, and K. N. Salama, "A CMOS RF-to-DC Power Converter With 86% Efficiency and 19.2-dBm Sensitivity," *IEEE Trans. Microw. Theory Techn.*, vol. 66, no. 5, pp. 2409–2415, 2018.

[4] Z. Zeng, S. Shen, X. Zhong, X. Li, C.-Y. Tsui, A. Bermak, R. Murch, and E. Sánchez-Sinencio, "Design of Sub-Gigahertz Reconfigurable RF Energy Harvester From 22 to 4 dBm With 99.8% Peak MPPT Power Efficiency," *IEEE J. Solid-State Circuits*, vol. 54, no. 9, pp. 2601–2613, 2019.

[5] X. Liao, Y. Zhang, Y. Zhang, S. Zhang, Z. Zhu, and L. Liu, "A High-Efficiency RFEH System With Feedback-Free Fast (F^3) MPPT Over a Wide Input Range," *IEEE Trans. Circuits Syst. I*, vol. 72, no. 6, pp. 2592–2602, 2025.
[6] Y. Park and S. Byun, "Analysis and Design of a 970-MHz, 108-Stage CMOS Ambient RF Energy Harvester With 36.5-dBm Input Power Sensitivity," *IEEE Trans. Microw. Theory Techn.*, vol. 72, no. 6, pp. 3829–3840, 2024.
[7] S. M. Noghabaei, R. L. Radin, Y. Savaria, and M. Sawan, "A High-Sensitivity Wide Input-Power-Range Ultra-Low-Power RF Energy Harvester for IoT Applications," *IEEE Trans. Circuits Syst. I*, vol. 69, no. 1, pp. 440–451, 2022.
[8] A. F. Yeknami, X. Wang, I. Jeerapan, S. Imani, A. Nikoofard, J. Wang, and P. P. Mercier, "A 0.3-V CMOS Biofuel-Cell-Powered Wireless Glucose/Lactate Biosensing System," *IEEE J. Solid-State Circuits*, vol. 53, no. 11, pp. 3126–3139, 2018.
[9] S. Choi, C. S. Park, H. Y. Chae, B. Oh, J. Lee, Y. M. Kwon, J. M. Baik, H. Shin, and J. J. Kim, "A Wide Dynamic Range Multi-Sensor ROIC for Portable Environmental Monitoring Systems With Two-Step Self-Optimization Schemes," *IEEE Trans. Circuits Syst. I*, vol. 68, no. 6, pp. 2432–2443, 2021.
[10] M. Pertijs, K. Makinwa, and J. Huijsing, "A CMOS Smart Temperature Sensor With a 3σ Inaccuracy of $\pm$0.1°C From -55°C to 125°C," *IEEE J. Solid-State Circuits*, vol. 40, no. 12, pp. 2805–2815, 2005.
[11] S. Pan, Y. Luo, S. Heidary Shalmany, and K. A. A. Makinwa, "A Resistor-Based Temperature Sensor With a 0.13 pJ · K2 Resolution FoM," *IEEE J. Solid-State Circuits*, vol. 53, no. 1, pp. 164–173, 2018.
[12] H. Park and J. Kim, "A 0.8-V Resistor-Based Temperature Sensor in 65-nm CMOS With Supply Sensitivity of 0.28 °C/V," *IEEE J. Solid-State Circuits*, vol. 53, no. 3, pp. 906–912, 2018.
[13] P. Chen, C.-C. Chen, C.-C. Tsai, and W.-F. Lu, "A Time-to-Digital-Converter-Based CMOS Smart Temperature Sensor," *IEEE J. Solid-State Circuits*, vol. 40, no. 8, pp. 1642–1648, 2005.
[14] K. Yang, Q. Dong, W. Jung, Y. Zhang, M. Choi, D. Blaauw, and D. Sylvester, "A 0.6nJ 0.22/+0.19°C Inaccuracy Temperature Sensor Using Exponential Subthreshold Oscillation Dependence," in *IEEE Int. Solid-State Circuits Conf. (ISSCC) Dig. Tech. Papers*, 2017, pp. 160–161.
[15] J. Li, B. Yao, L. Fan, T. Zhang, Y. Zhang, K. Wu, Z. Zhang, Q. Zhang, Y. Wang, N. Ning, and Q. Yu, "A 20 nW +0.8°C/-0.8°C Inaccuracy (3σ) Leakage-Based CMOS Temperature Sensor With Supply Sensitivity of 0.9°C/V," *IEEE Trans. Circuits Syst. I*, vol. 70, no. 8, pp. 3142–3153, 2023.
[16] S. Jeong, Z. Foo, Y. Lee, J.-Y. Sim, D. Blaauw, and D. Sylvester, "A Fully-Integrated 71 nW CMOS Temperature Sensor for Low Power Wireless Sensor Nodes," *IEEE J. Solid-State Circuits*, vol. 49, no. 8, pp. 1682–1693, 2014.
[17] Z. Tang, Y. Fang, Z. Shi, X.-P. Yu, N. N. Tan, and W. Pan, "A 1770-μm^2 Leakage-Based Digital Temperature Sensor With Supply Sensitivity Suppression in 55-nm CMOS," *IEEE J. Solid-State Circuits*, vol. 55, no. 3, pp. 781–793, 2020.
[18] H. Bhamra, Y.-J. Kim, J. Joseph, J. Lynch, O. Z. Gall, H. Mei, C. Meng, J.-W. Tsai, and P. Irazoqui, "A 24 μW, Batteryless, Crystal-free, Multinode Synchronized SoC "Bionode" for Wireless Prosthesis Control," *IEEE J. Solid-State Circuits*, vol. 50, no. 11, pp. 2714–2727, 2015.
[19] J. Yin, J. Yi, M. K. Law, Y. Ling, M. C. Lee, K. P. Ng, B. Gao, H. C. Luong, A. Bermak, M. Chan, W.-H. Ki, C.-Y. Tsui, and M. Yuen, "A System-on-Chip EPC Gen-2 Passive UHF RFID Tag With Embedded Temperature Sensor," *IEEE J. Solid-State Circuits*, vol. 45, no. 11, pp. 2404–2420, 2010.
[20] M. Song, Y. Huang, H. J. Visser, J. Romme, and Y.-H. Liu, "An Energy-Efficient and High-Data-Rate IR-UWB Transmitter for Intracortical Neural Sensing Interfaces," *IEEE J. Solid-State Circuits*, vol. 57, no. 12, pp. 3656–3668, 2022.
[21] J. Lei, X. Liu, W. Song, H. Huang, X. Ma, J. Wei, and M. Zhang, "Design of a Low-Power, High-Data-Rate, and Crystal-Less All-Digital IR-UWB Transmitter for High-Density Neural Implants," *IEEE J. Solid-State Circuits*, vol. 59, no. 7, pp. 2159–2170, 2024.
[22] D. Bao, Z. Zou, M. Baghaei Nejad, Y. Qin, and L.-R. Zheng, "A Wirelessly Powered UWB RFID Sensor Tag With Time-Domain Analog-to-Information Interface," *IEEE J. Solid-State Circuits*, vol. 53, no. 8, pp. 2227–2239, 2018.
[23] Y. Luo, Y. Li, A. V.-Y. Thean, and C.-H. Heng, "A 70-μW 1.35-mm^2 Wireless Sensor With 32 Channels of Resistive and Capacitive Sensors and Edge-Encoded PWM UWB Transceiver," *IEEE J. Solid-State Circuits*, vol. 56, no. 7, pp. 2065–2076, 2021.
[24] C. E. Rasmussen and C. K. I. Williams, *Gaussian Processes for Machine Learning*. The MIT Press, 11 2005. [Online]. Available: https://doi.org/10.7551/mitpress/3206.001.0001
[25] H. S. Ozturk, J. Arenas, C. Tokunaga, N. Kurd, and V. Sathe, "8.7 A Dual VDD-Temperature Sensor Employing Sensor Fusion with 2.4°C, 9mV ($\pm 3\sigma$) Inaccuracy in 65nm CMOS," in *IEEE Int. Solid-State Circuits Conf. (ISSCC) Dig. Tech. Papers*, vol. 68, 2025, pp. 170–172.
[26] I. Filanovsky and A. Allam, "Mutual Compensation of Mobility and Threshold Voltage Temperature Effects with Applications in CMOS Circuits," *IEEE Trans. Circuits Syst. I*, vol. 48, no. 7, pp. 876–884, 2001.
[27] I. Lee, D. Sylvester, and D. Blaauw, "A Subthreshold Voltage Reference With Scalable Output Voltage for Low-Power IoT Systems," *IEEE J. Solid-State Circuits*, vol. 52, no. 5, pp. 1443–1449, 2017.
[28] W. Wang, B. Zhu, Y. Xuan, Y. Shen, Q. Xiao, Z. Wang, Y. Luo, G. Pan, B. Su, and B. Zhao, "A Wireless Battery-Free Cerebral-Oxygen-Monitoring Micro-System Featuring 0.21-mmHg Sensing Resolution," *IEEE J. Solid-State Circuits*, vol. 60, no. 10, pp. 3538–3550, 2025.
[29] M. Privitera, A. Ballo, K. Ali, A. Dario Grasso, and M. Alioto, "Sub-μW Battery-Less and Oscillator-Less Wi-Fi Backscattering Transmitter Reusing RF Signal for Harvesting, Communications, and Motion Detection," *IEEE J. Solid-State Circuits*, vol. 60, no. 6, pp. 1947–1958, 2025.
[30] H. Zhang, W.-H. Yu, Z. Yang, K.-F. Un, J. Yin, R. P. Martins, and P.-I. Mak, "A 90.7-nW Vibration-Based Condition Monitoring Chip Featuring a Digital Compute-in-Memory-Based DNN Accelerator Using an Ultra-Low-Power 13T-SRAM Cell," *IEEE J. Solid-State Circuits*, vol. 60, no. 1, pp. 321–331, 2025.
[31] Z. Li, C. Yang, Y. Zhang, T.-H. Wang, Z. Chang, B. Zhu, L. Zhou, Y. Luo, B. Su, and B. Zhao, "A 1 mm × 1 mm CGM System on Die Achieving 1.65-nA/mM In Vivo Resolution and 0–40-mM/L Detection Range With $\Delta\Sigma$ Backscatter Technique," *IEEE J. Solid-State Circuits*, vol. 58, no. 7, pp. 2053–2063, 2023.
[32] C. Jeon, J. Koo, K. Lee, M. Lee, S.-K. Kim, S. Shin, S. K. Hahn, and J.-Y. Sim, "A Smart Contact Lens Controller IC Supporting Dual-Mode Telemetry With Wireless-Powered Backscattering LSK and EM-Radiated RF Transmission Using a Single-Loop Antenna," *IEEE J. Solid-State Circuits*, vol. 55, no. 4, pp. 856–867, 2020.
[33] P. Saffari, A. Basaligheh, V. J. Sieben, and K. Moez, "An RF-Powered Wireless Temperature Sensor for Harsh Environment Monitoring With Non-Intermittent Operation," *IEEE Trans. Circuits Syst. I*, vol. 65, no. 5, pp. 1529–1542, 2018.



Martin Lee received the B.Sc. and M.Sc. degrees in electrical engineering from the University of Alberta, Edmonton, AB, Canada, in 2017 and 2020, respectively. He is currently pursuing the Ph.D. degree in electrical engineering at the University of Alberta, Edmonton, AB, Canada. His major research interests include the design of analog, radio frequency and PVT-invariant CMOS integrated circuits and systems.



Kambiz Moez (S'01-M'07-SM'12) received his B.Sc. degree in electrical engineering from the University of Tehran, Iran, in 1999, and his M.Sc. and Ph.D. degrees from the University of Waterloo, Waterloo, Ontario, Canada, in 2002 and 2006, respectively. Since January 2007, he has been with the Department of Electrical and Computer Engineering, University of Alberta, Edmonton, AB, Canada, where he is currently a Professor and Associate Dean of Undergraduate Students - ECE. His research interests include the analysis and design of analog, radio frequency, and millimeter-wave CMOS integrated circuits and systems for a variety of applications, including wired/wireless communications and sensors, radio frequency energy harvesting, biomedical imaging, instrumentations, radars, and power electronics. He has authored or co-authored over 110 peer-reviewed journal articles and conference papers in his field of research. Dr. Moez is a Registered Professional Engineer in the province of Alberta. Dr. Moez served as Associate Editor for IEEE Transactions on Circuits and Systems I: Regular Papers from 2021 to 2023. He is currently serving as an Associate Editor for IET Electronics Letters.